## Title

Ba promoter effect on cobalt-catalyzed ammonia decomposition kinetics: A theoretical analysis



## Authors

Almisbaa, Zahra
Sautet, Philippe

## Publication Date

2024

## DOI

10.1016/j.jechem.2024.07.0502095-4956

# Ba promoter effect on cobalt-catalyzed ammonia decomposition kinetics: A theoretical analysis

Zahra Almisbaa [a], Philippe Sautet [a,b]*

[a] *Department of Chemical and Biomolecular Engineering, University of California, Los Angeles, Los Angeles, California 90095, United States*

[b] *Department of Chemistry and Biochemistry, University of California, Los Angeles, Los Angeles, California 90095, United States*

*Corresponding author.

*E-mail address:* sautet@ucla.edu (P. Sautet).

## ABSTRACT

Ammonia decomposition is a key reaction in the context of hydrogen storage, transport, and release. This study combines density functional theory (DFT) calculations with microkinetic modeling to address the promotion mechanism of Ba species for ammonia decomposition on Co catalysts. The modified adsorption properties of Co upon the addition of metallic Ba or BaO suggest that the promoters play a role in alleviating the competitive adsorption of H. Calculating the full reaction pathway of ammonia decomposition shows that limiting the investigation to the N–N association step, as done previously, overlooks the effect of the promoter on the energy barriers of the $NH_x$ dehydrogenation steps. Challenges of modeling the ammonia decomposition reaction are addressed by understanding that the $NH_2$ intermediate is stabilized on the step sites rather than the terrace sites. When the effect of H-coverage on the adsorption of $NH_3$ is not considered in the microkinetic simulations, the results conflict with the experiments. However, accounting for the effect of H-coverage, as performed here, shows that BaO-doped Co has higher

rates than pristine Co and Ba-doped Co at the reaction temperature of 723.15 K. When H is adsorbed on the Ba-doped Co, the adsorption of ammonia becomes significantly endergonic, which makes the rates relatively slow. The superiority of the BaO-promoted catalyst is attributed to a lower energy for the transition state of the rate-determining step, coupled with a reduced impact of the hydrogen coverage on weakening the ammonia adsorption. The kinetic analysis of the influence of Ba and BaO on the Co surface shows that BaO-doped Co aligns more closely with experimental observations than Ba-doped Co. This implies that Ba on the Co surface is likely to be in an oxide form under reaction conditions. Understanding the kinetics of the ammonia decomposition reaction provides a foundation for developing highly effective catalysts to accelerate the industrial utilization of ammonia as a sustainable hydrogen carrier.

*Keywords:* Cobalt catalyst; Ammonia decomposition; Hydrogen carrier; DFT; Microkinetic

## 1. Introduction

Thermocatalytic ammonia decomposition is widely recognized as a promising process to produce hydrogen due to the high hydrogen storage capacity (17.7 wt%) of ammonia and the well-established production, storage, and distribution infrastructures [1–7]. Ammonia decomposition is the reverse of the Haber-Bosch reaction, and it involves breaking down ammonia into its constituent elements of hydrogen and nitrogen using a catalyst [7]. The hydrogen generated by this process has a high level of purity, as it is the only product formed along with molecular nitrogen [6]. On an industrial scale, hydrogen is currently produced through steam methane reforming coupled with the water-gas shift reaction, which is responsible for large amounts of carbon dioxide emissions [4–7]. Ammonia decomposition, on the other hand, is a carbon-free source for hydrogen generation [6–8]. These reasons have fueled a growing interest in studying the ammonia decomposition reaction.

The reaction occurs at atmospheric pressure and typically requires a temperature of 500 °C and higher to achieve complete conversion of ammonia [4,7,9]. Achieving full conversion is critical to avoid the need for subsequent purification, which would add expenses and compromise the efficiency of the process [4,5]. At a temperature lower than 400 °C, conversion is limited by thermodynamic equilibrium. On the other hand, a high operating temperature does not comply with the U.S. DOE hydrogen storage requirement and poses a great risk for the onsite hydrogen production [10,11]. Therefore, a catalyst that can reach a high conversion at a temperature lower than 500 °C is important for making ammonia decomposition a safe and economically feasible method for hydrogen generation.

Ru-based catalysts have shown superior activity in decomposing ammonia and have been extensively studied experimentally and theoretically [5,12–17]. However, the high cost and the scarcity of Ru limit the process from becoming viable for large-scale hydrogen production. Therefore, there is a need to find a noble metal-free catalyst that can facilitate a complete conversion of ammonia in conditions preferably under 500 °C [9,18].

Co-based catalysts have received intense interest as scalable and cost-effective alternatives for Ru-based catalysts [18–20]. In a recent study by the Gascon group, the catalytic activity of Ba-promoted Co was found to be comparable to the K-promoted Ru benchmark at 500 °C [9]. Metallic Co was identified as the active phase for the reaction [9,18]. Experimental characterization showed that the crystal phase of the Co under reaction conditions was mainly hexagonal close-packed (HCP) [9]. The superior catalytic activity of the HCP phase in comparison to the face-centered cubic (FCC) phase was attributed to the presence of denser active sites in the HCP phase [21,22]. Research has established that B5 sites on the B-type step are critical active sites for driving the ammonia synthesis and decomposition reactions

[12,13,22–24]. B5 sites are the specific arrangement of two atoms on the B-type step edge and three atoms on the lower terrace [25]. The distribution of the B5 sites differs significantly between the HCP and the FCC phase, which translates into different catalytic activity [22].

While metallic Co was confirmed as the active site, the Ba-based promoter was found to influence the kinetics of the reaction by enhancing the rate of $N_2$ association alongside the $NH_x$ dehydrogenation steps [26]. Experiments show that Co-based catalysts exhibit strong hydrogen adsorption, leading to poisoning of the active sites on the surface. This is evidenced by the negative reaction order with respect to hydrogen, as also seen in Ru and Ni catalysts [4,27–30]. However, catalysts with Ba-based promoters exhibited a less negative reaction order in comparison to the non-promoted Co catalysts [9,26]. A similar observation was found with high entropy alloys containing Co and Mo when Mo-rich alloys showed less hydrogen inhibition effect [20]. A study by He et al. also mentioned that bimetallic NiCo catalysts showed less hydrogen poisoning in comparison to monometallic Ni and Co [31]. Moreover, Srifa et al. and Kishida et al. proved that introducing Cs on $Co_3Mo_3N$ and Ru catalysts mitigated the impact of hydrogen poisoning on the active sites of the catalysts [17,19]. Even though the negative influence of the strong hydrogen adsorption during the ammonia decomposition reaction has been proven experimentally, the understanding of how promoters reduce the hydrogen competitive adsorption and the effects of hydrogen coverage is still limited and rarely addressed in theoretical studies.

However, recent theoretical studies shed light on how promoters modify the catalytic surface. Cao et al. identified an effect induced by metallic promoters on spin-polarized catalysts including Co [32]. While the promoter effect on Ru was mainly attributed to electrostatic dipole interactions, the promoter effect on Co was ascribed to reduction in spin polarization in addition

to electrostatic effect [32]. When Co was promoted with metallic Li, Ba, Ca, and La, the neighboring Co atoms experienced a decrease in their spin moment [33]. This decrease is not only induced by promoters but also by adsorbates. Qian et al. observed a decrease in the spin moment of Fe catalysts induced by reactants and intermediates during ammonia synthesis [34]. The change in spin moment was the highest for N, and it decreased with a smaller magnitude for H, NH, and $NH_2$ to form $NH_3$. This reduction in spin polarization created by specific adsorbates or promoters has not been fully explored and it holds great significance in tuning the catalytic activity of ferromagnetic metals [32,33,35].

Here, we present a density functional theory (DFT)-based investigation of the kinetic influence of metallic Ba and BaO on Co catalysts during the ammonia decomposition reaction. We aim to address fundamental questions that have not been clarified or accounted for in prior studies. (i) How dose Ba/BaO alleviate the competitive adsorption of hydrogen during the reaction? (ii) How does the reaction kinetics differ with the nature of the promoter (metallic or oxidized)? (iii) What is the electronic origin that dictates the promotion effect of each promoter? Exploring these questions paves the way for developing highly efficient catalysts and accelerating the industrial utilization of ammonia as a sustainable hydrogen carrier.

## 2. Methods

### *2.1. DFT methods*

Spin-polarized DFT calculations were performed using the Vienna Ab-initio Simulation Package (VASP) [36,37]. Custom Python scripts from GitHub were used to automate VASP functionalities [38]. Core electrons were described by the projector-augmented wave (PAW) method, while valence electron orbitals were developed in a basis set of plane waves with a 400 eV cutoff energy [39,40]. Electronic structures were calculated using the Perdew-Burke-Ernzerhof (PBE) exchange-correlation functional in the framework of the generalized gradient approximation (GGA) [41]. Dispersion interactions were included using the DFT-D3 method of Grimme [42,43]. The force convergence threshold was set to be 0.03 eV/Å.

HCP bulk Co with *P*63/*mmc* crystallographic symmetry and two Co atoms per unit cell was optimized using a Monkhorst-Pack *k*-point mesh of (10×10×6). The calculated lattice constants are $a = b$ =2.466 Å and $c$ = 3.987 Å, which are consistent with experimental values ($a = b$ = 2.507 Å and $c$ = 4.061 Å) [21,22,44,45]. The stepped $(10\bar{1}5)$ facet was selected because of the presence of the B5 sites, which are essential to activate N–N association [25,46,47]. Also, the $(10\bar{1}5)$ facet of HCP Co has the strongest H adsorption relative to other facets, making it suitable for investigating the competitive adsorption of H [47]. Surfaces were modeled by 4×6 supercells and four-atomic-layer slabs [25]. Top and side views of the studied surfaces are shown in Fig. 1. The large atomic radius of Ba in comparison to Co means that Ba is likely to be located on the surface of the system. The positions of the two topmost layers and the adsorbates were relaxed, and the rest of the layers were fixed to the bulk geometry. Sampling of the Brillouin zone was performed by a (5×5×1) Monkhorst-Pack grid [48]. Periodic slabs were separated in the vertical ($z$) direction by a 15 Å vacuum gap and the dipole correction was applied. The climbing image-

nudged elastic band (CI-NEB) method [49] with 8 images was used for transition state calculations. Structures and energies of transition states were subsequently converged to low force (0.03 eV/Å) using the Quasi-Newton method. Transition states were verified using vibrational frequency calculations, resulting in a single imaginary frequency along the reaction coordinate.

In the following, the bare Co surface will be referred to as (Co). Ba doping is modelled by the adsorption of a single Ba atom on the unit cell called (Co-Ba), while BaO doping is modelled by a single BaO unit on the unit cell called (Co-BaO). Modeling single-atom promoters, rather than nanoparticles, is a computationally reasonable approach that was found to yield accurate results, particularly for $NH_3$ synthesis or dehydrogenation reactions [25,32,33,50]. This simple model isolates the role of the promoter and effectively captures the surface interactions without the added complexities of multiple promoter atoms interacting with each other and with the surface.

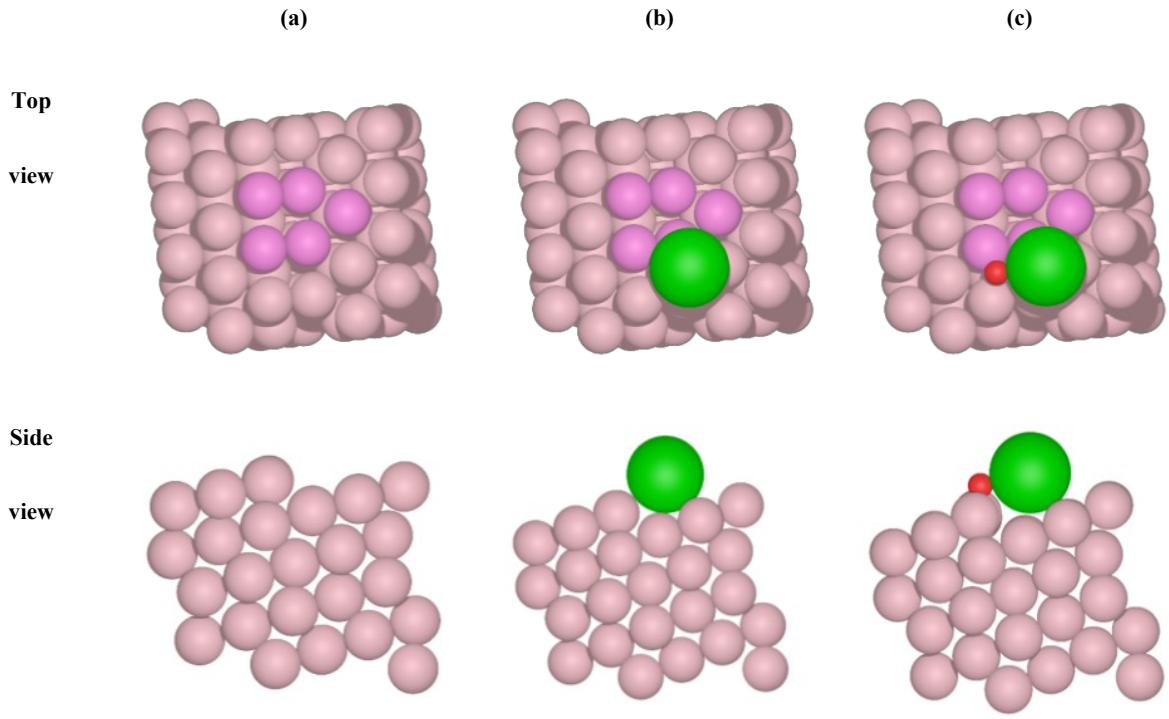


**Fig. 1.** Top and side views of Co, Co-Ba, and Co-BaO model catalysts. Surfaces were constructed from 4×6 supercells of the Co $(10\bar{1}5)$ surface, involving four-atomic layers. Co atoms in the B5 sites are highlighted. Color code: Co (pink), B5 site (purple), Ba (green), and O (red).

The internal adsorption energy of adsorbates ($NH_3$*, $NH_2$*, NH*, H*, and N*) was calculated following Eq. (1).

$$\Delta E_{\text{adsorption}} = E_{\text{adsorbate/surface}} - E_{\text{surface}} - E_{\text{adsorbate}} \quad (1)$$

Where $\Delta E_{\text{adsorption}}$ is the adsorption energy, $E_{\text{adsorbate/surface}}$ is the total energy of the adsorbates on the surface of the slab, $E_{\text{surface}}$ is the energy of the clean slab surface, and $E_{\text{adsorbate}}$ is the energy of the reference gaseous molecules.

The Gibbs free energy for reactants and intermediates adsorbed on the surface was calculated according to Eq. (2) while treating all vibrational degrees of freedom harmonically.

$$G = E + E_{vib} + PV - TS \quad (2)$$

where $G$ is Gibbs free energy, $E$ the internal energy, and $E_{vib}$ is the vibrational energy of the system calculated using the atomic simulation environment (ASE) package [51]. The pressure and volume ($PV$) term is assumed to be negligible. $T$ is the reaction temperature (723.15 K) and $S$ is the entropy including only the vibrational degrees of freedom for the adsorbates. In certain scenarios, the change of Gibbs free energy ($\Delta G$) values was approximated assuming that vibrational contributions were negligible. Translational, rotational, electronic, and vibrational degrees of freedom were included for the gas phase molecules. Gas phase thermodynamics and Gibbs free energy of Co-promoted surfaces under reaction conditions are presented in Table S1 and Fig. S1, respectively.

*2.2. Microkinetic model*

The microkinetic model was constructed based on the six elementary steps presented in Table 1 with no assumption of a rate-determining step. An initial conversion value of 15% was employed assuming an atmospheric pressure for $NH_3$. The model included the reaction constants of the adsorption, desorption, and surface reaction steps determined using the free energy values obtained from DFT calculations. The resulting system of ordinary differential equations was solved till a steady state was reached. The backward-differentiation formulas (BDF) method was used which is fit for solving a set of stiff differential equations as implemented in the Python package SciPy [52].

The maximum H coverage on Co, Co-Ba, and Co-BaO slabs corresponds to 24, 20, and 18 H atoms, respectively. This is assuming 1 H atom per accessible Co atom on the 4×6 unit cell, as Ba and BaO block some of the adsorption sites. The configurations of H at various coverages were generated manually. While the configurations could have been sampled in more detail with

exhaustive global optimization techniques, these approaches are highly computer-intensive for large spin-polarized systems.

To incorporate the coverage effect of H in the surface unit cell, initial coverages of 18 adsorbed H (0.75 ML) for Co, 12 adsorbed H (0.60 ML) for Co-Ba, and 14 adsorbed H (0.78 ML) for Co-BaO were used in the microkinetic model. These coverages were selected because they are the most thermodynamically stable coverages if two additional H atoms are adsorbed. Notably, the decision to refrain from selecting the most thermodynamically stable coverage as the initial state is to allow for both adsorption and desorption reactions to take place. Opting for the most stable coverage would have exclusively favored desorption over adsorption during Step 6 of the elementary steps presented in Table 1. Steps 1 and 6 assume a barrierless adsorption/desorption, and our calculations show that they are the only two relevant steps that are significantly coverage-dependent. $\Delta G^{\ddagger}$ for the surface reaction steps is assumed to be unchanged by H coverage. This is based on the observation that the presence of H coverage does not impact the value of energy barriers as it has a similar effect on the initial and the final states of the transition states.

A single-site model assumes only one type of active site on the catalyst surface, where all reaction steps happen on this single, uniform type of site. When applying this model, the coverage of $NH_2$* is overestimated. To address this challenge, a two-site model was used to account for the presence of different types of active sites where 0.16 ML of the surface sites is step-type and 0.84 ML is terrace-type. A similar concept was utilized by Vojvodic et al. to tackle the issue of overestimating $NH_2$* coverage in the ammonia synthesis reaction [53]. H and N can be adsorbed on both types of sites, while all the $NH_x$ species are adsorbed on step sites only.

These assumptions were made based on the calculated stability of the adsorbed species on both types of sites.

For the surface reaction steps, the rate constants were calculated according to the conventional transition state theory in Eq. (3).

$$k = \frac{\mathrm{k_B}T}{\mathrm{h}} e^{-\Delta G^{\ddagger}/\mathrm{k_B}T} \tag{3}$$

where $k_B$ is the Boltzmann constant, $T$ is the reaction temperature, h is Planck's constant, and $\Delta G^{\ddagger}$ is the free energy difference between the transition state and the most stable configuration of the initial state.

All the reaction constants $k$ values were expressed in $s^{-1}$. The $NH_3$ and H adsorption steps in Table 1 were assumed to be non-activated and the rate constants were obtained from the kinetic theory of gases as shown in Eq. (4).

$$k_{\mathrm{adsorption}} = \frac{\sigma P^0 A}{\sqrt{2\pi m \mathrm{k_B}T}} \tag{4}$$

Where $\sigma$ is the initial sticking probability taken here as 1, $P^{\circ}$ is the standard pressure, and $m$ is the mass of the adsorbate. $A$ is the surface area for one active site and a typical value of $10^{-19}$ $m^2$ was used here [54,55]. Desorption rate constants were calculated from the adsorption equilibrium constant, $K_{\mathrm{adsorption}}$ was the rate constant for adsorption as shown in Eq. (5).

$$k_{\mathrm{desorption}} = \frac{k_{\mathrm{adsorption}}}{K_{\mathrm{adsorption}}} \tag{5}$$

**Table 1**

Elementary steps and rate equations used in the microkinetic model. Step sites and terrace sites are distinguished. [a,b]

| | Surface reaction | Rate equation |
|---|---|---|
| **1** | $NH_3(g) + * \leftrightarrow NH_3*$ | $r_1 = k_1\theta_* P_{NH_3} / P^o - k_{-1}\theta_{NH_3*}$ |
| **2** | $NH_3^* + \delta \leftrightarrow NH_2^* + H^\delta$ | $r_2 = k_2\theta_{NH_3*}\theta_\delta - k_{-2}\theta_{NH_2*}\theta_{H\delta}$ |
| **3** | $NH_2^* + \delta \leftrightarrow NH^* + H^\delta$ | $r_3 = k_3\theta_{NH_2*}\theta_\delta - k_{-3}\theta_{NH*}\theta_{H\delta}$ |
| **4(a)** | $NH^* + \delta \leftrightarrow N^* + H^\delta$ | $r_{4(a)} = k_4\theta_{NH*}\theta_\delta - k_{-4}\theta_{N*}\theta_{H\delta}$ |
| **4(b)** | $NH^* + \delta \leftrightarrow N^\delta + H^*$ | $r_{4(b)} = k_4\theta_{NH*}\theta_\delta - k_{-4}\theta_{N\delta}\theta_{H*}$ |
| **5** | $N^* + N^\delta \leftrightarrow N_2(g) + * + \delta$ | $r_5 = k_5\theta_{N*}\theta_{N\delta} - k_{-5}\theta_*\theta_\delta P_{N_2} / P^o$ |
| **6(a)** | $2\,H^\delta \leftrightarrow H_2(g) + 2\,\delta$ | $r_{6(a)} = k_6\theta_{H\delta}^2 - k_{-6}\theta_\delta^2 P_{H_2} / P^o$ |
| **6(b)** | $2\,H^* \leftrightarrow H_2(g) + 2\,*$ | $r_{6(b)} = k_6\theta_{H*}^2 - k_{-6}\theta_*^2 P_{H_2} / P^o$ |

[a] * represents the free step site on the surface.

[b] $\delta$ represents the free terrace site on the surface.

## 3. Results and discussion

### *3.1. Coverage-dependent H adsorption*

Exploring how the adsorption energy of H varies with coverage is important to understand the population of surface species under reaction conditions. It was previously reported that H is the most abundant species on the surface during the ammonia decomposition reaction [26,56,57]. Fig. 2 presents the Gibbs free energies of N, $NH_3$, and H adsorbed at low coverage on the most stable sites of Co, Co-Ba, and Co-BaO at the reaction temperature. The configurations of the adsorbates are provided in Table S2. Calculations show that Co-Ba has the strongest adsorption energies for N and H, while Co has the strongest adsorption for $NH_3$. However, these adsorption energies are calculated on bare surfaces and, thus, do not indicate the dominating species during a steady state of the reaction. The small size of H atoms, their weak lateral interactions between adsorbates, and their mobility can make them more likely to accumulate on the surface and reach a high-coverage situation per catalyst unit surface area.

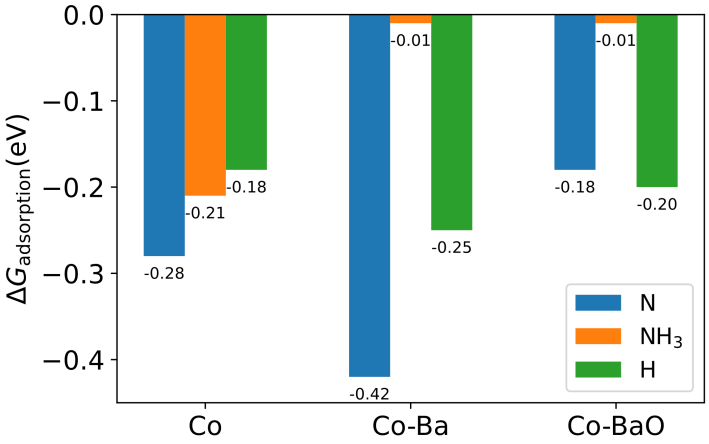


**Fig. 2.** Gibbs free energies of N, $NH_3$, and H absorbed on Co, Co-Ba, and Co-BaO at 723.15 K. The reference is bare surface and $H_2$(g), $N_2$(g), or $NH_3$(g) for each species accordingly. These

adsorption energies at low coverage do not reflect the dominating species during a steady state of the reaction.

Fig. 2 shows that the adsorption energy of one H atom varies only slightly between the three surfaces. However, the difference in energy becomes pronounced when multiple H atoms are adsorbed on the surface. Fig. 3 shows the Gibbs free energy of adsorbed H as a function of H coverage at 723.15 K, which is the target reaction temperature. The adsorption of H is weakened after a certain threshold coverage is reached. The number of adsorbed H corresponding to the most negative Gibbs free energy, which is the equilibrium coverage, varies depending on the surface (24 H for Co, 20 H for Co-Ba, and 18 H for Co-BaO for the unit cell). This is because Ba and BaO block some of the adsorption sites. Co and Co-Ba exhibit the strongest total adsorption Gibbs free energy at equilibrium, while Co-BaO shows a markedly weaker H adsorption free energy. If the investigation was solely focused on the adsorption of a single H atom (Fig. 2), the conclusions could be misleading. This observation highlights the importance of studying the coverage effect on adsorption energies.

The trend toward H adsorption was further confirmed when H atoms were adsorbed at identical sites across every surface, as shown in Fig. S2. The average chemisorption energies as a function of coverage are provided in Fig. S3. Fig. 3 and Figs. S2 and S3 gave the same conclusion and the order of absolute values of H binding energy is Co-BaO < Co < Co-Ba.

The modified adsorption properties of Co upon the addition of metallic Ba or BaO suggest that BaO plays a role in alleviating the competitive adsorption of H. The weakened adsorption energies on Co-BaO may translate into higher desorption rates of H and more availability of active sites on the catalytic surface. This finding helps in understanding the experimental observation of reduced competitive adsorption of H on Ba-based promoted

catalysts in comparison to unpromoted Co, which has not been explained in the literature. This also suggests that the catalytically active phase is associated with BaO doping rather than metallic Ba and the oxidic nature of BaO is preserved under reaction conditions. Cao et al. have mentioned that the nature of the precursor on the Co catalyst might affect the active sites because it could be challenging to reduce the precursors [32].

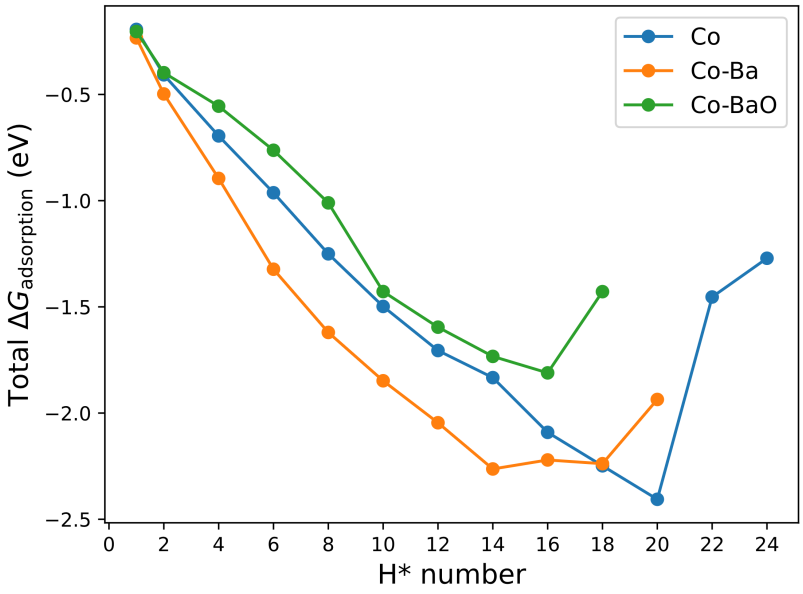


**Fig. 3.** Total chemisorption free energies at 723.15 K versus the number of adsorbed H atoms on Co, Co-Ba, and Co-BaO. The reference is bare surface and $H_2$(g). Change of Gibbs free energy ($\Delta G$) values was approximated assuming that vibrational contributions were negligible. The generated geometries and the values of adsorption energies are presented in Tables S3–S5. The adsorption of H is significantly weakened after reaching a certain threshold. The threshold (equilibrium) coverage corresponds to a different number of adsorbed H on each surface. The weaker adsorption strength for the Co-BaO surface becomes evident when multiple H atoms are adsorbed, in contrast with the behavior observed on bare surfaces (Fig. 2).

Due to the small size of H atoms and the negligible repulsive interactions between them, the behavior of the coverage-dependent binding energies for H is different from that of larger adsorbates, e.g. $C_2H_2$ [58]. While molecules like $C_2H_2$ show a gradual decrease in the adsorption energy after a certain threshold, H binding energy is maintained until reaching equilibrium coverage where it tends to destabilize drastically as shown in Fig. 3. The possibility of surface restructuring at high coverage of H was not explored here, as it requires specific global optimization calculations which are outside the scope of this study.

*3.2. Reaction profiles*

The initial focus of this study is to understand the reaction on bare surfaces, setting the foundation to examine the H coverage effect in the next sections. Reaction profiles were calculated to provide insights into the adsorption properties and activation barriers of individual molecules. The reaction profiles on Co, Co-Ba, and Co-BaO are presented in Fig. 4. The values of all the energy barriers used in Fig. 4 and the structures of the transition states are shown in Tables S6–S9. The reaction starts with the adsorption of $NH_3$ on a bare surface followed by sequential dehydrogenation to generate H and N. The pathway has three N–H bond-breaking barriers (associated with transition states TS1, TS2, and TS3) and it ends with N–N and H–H association and desorption. TS4 corresponds to the N–N association barrier while the H–H association was reported to have negligible barrier [47]. The largest energy barrier for all the surfaces is for the N–N association step (Fig. 4 and Table S6). This is consistent with the existing literature proposing that the N–N association is the rate-determining step for many $NH_3$ decomposition catalysts [20,26]. Co has the highest transition state energy for N–N association (TS4), followed by Co-BaO and Co-Ba, indicating the promotional effect of Ba species on this step. A decrease of 0.17 eV in the free energy of the transition state was also observed for the

second N–H bond breaking for Co-Ba relative to Co. The dehydrogenation step of $NH_2$ was reported to be another kinetically relevant step in this reaction [26]. Studying the full reaction pathway clarified that limiting the investigation to the N–N association step overlooks the promotional effect on the energy barriers of the $NH_x$ dehydrogenation steps.

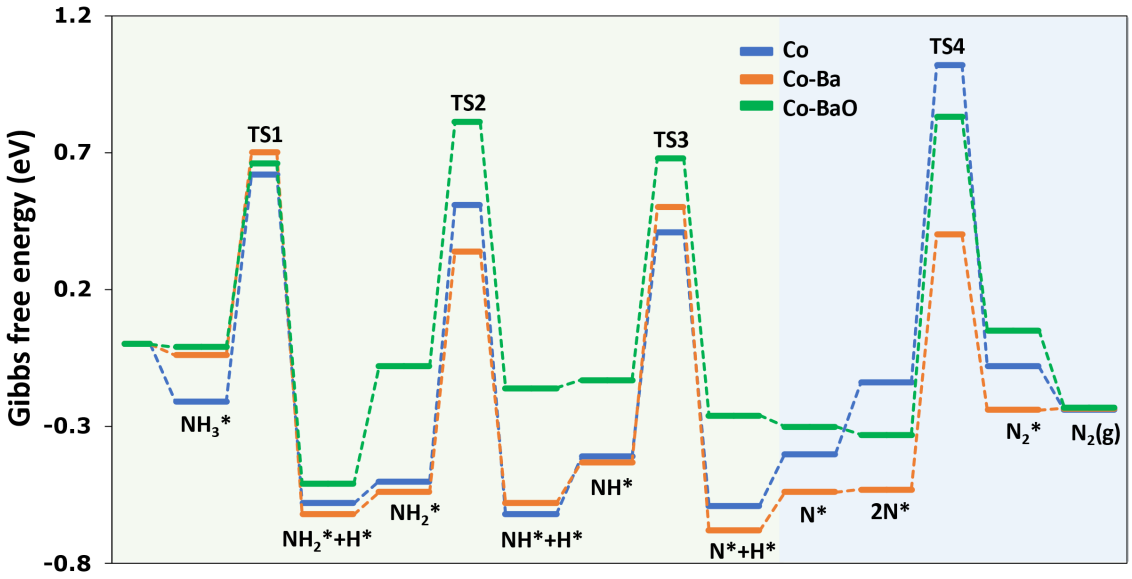


**Fig. 4.** Gibbs free energy profiles for ammonia decomposing on a bare surface of Co, Co-Ba, and Co-BaO at 723.15 K. Energies are relative to the bare surface, $NH_3$(g), and $H_2$(g). The labels assigned to each step denote the corresponding reacting species. The green region indicates the $NH_x$ dehydrogenation steps, and the blue region indicates the $N_2$ dissociation step.

*3.3. Microkinetic simulations*

Microkinetic simulations were performed to see how the reaction kinetics differ with the nature of the promoter (metallic or oxidized). Fig. 5 presents the $H_2$ production rates for the Co, Co-Ba, and Co-BaO catalysts across a range of temperatures. Co exhibits the highest rate at all temperatures, while Co-BaO has a consistently lower rate compared to both Co and Co-Ba. All the rates are converging at high temperatures. However, these results contrast with experimental

findings where Ba/BaO is introduced as a promoter, and thus, expected to show higher production rates than Co.

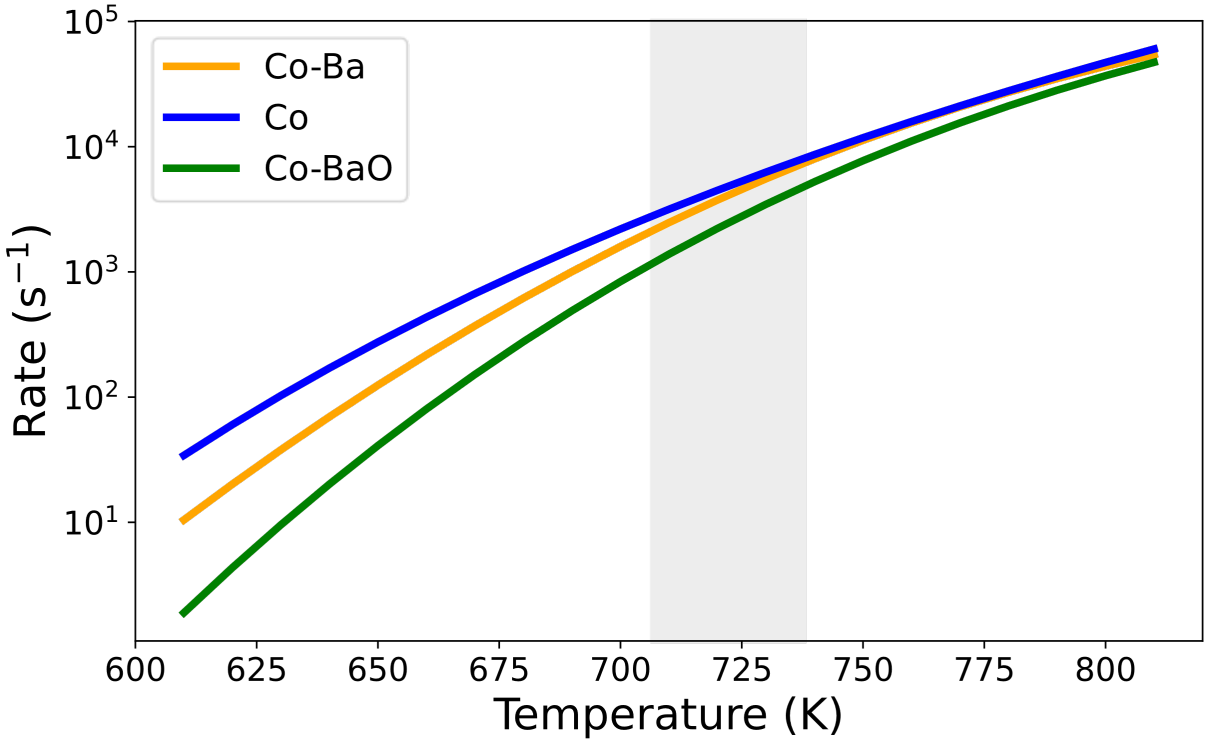


**Fig. 5.** $H_2$ production rates ($s^{-1}$) of Co, Co-Ba, and Co-BaO versus temperature (K) at 15% conversion. The simulations are obtained for ammonia decomposing on a bare surface. The gray shaded area indicates the reaction temperature (723.15 K). Co exhibits the highest rate compared to Ba-promoted surfaces. These results do not agree with experiments.

The coverage distribution of reaction species was then analyzed to understand the influence of Ba and BaO on the catalyst surface. Fig. 6 presents the calculations for surface coverage distributions at various temperatures and two conversion values. At 15% conversion, N is the dominant species on the surface for Co and Co-BaO, while H is the dominant species for Co-Ba. However, as the reaction progresses and at a higher conversion value (40% conversion), N remains the dominant species for Co but H becomes the dominant species for Co-BaO. For

Co-Ba, H continues to be the dominant species as shown in Fig. 6(d–f). This is supported by the results in Fig. 2, as H is adsorbed more strongly on Co-Ba than on Co-BaO and Co.

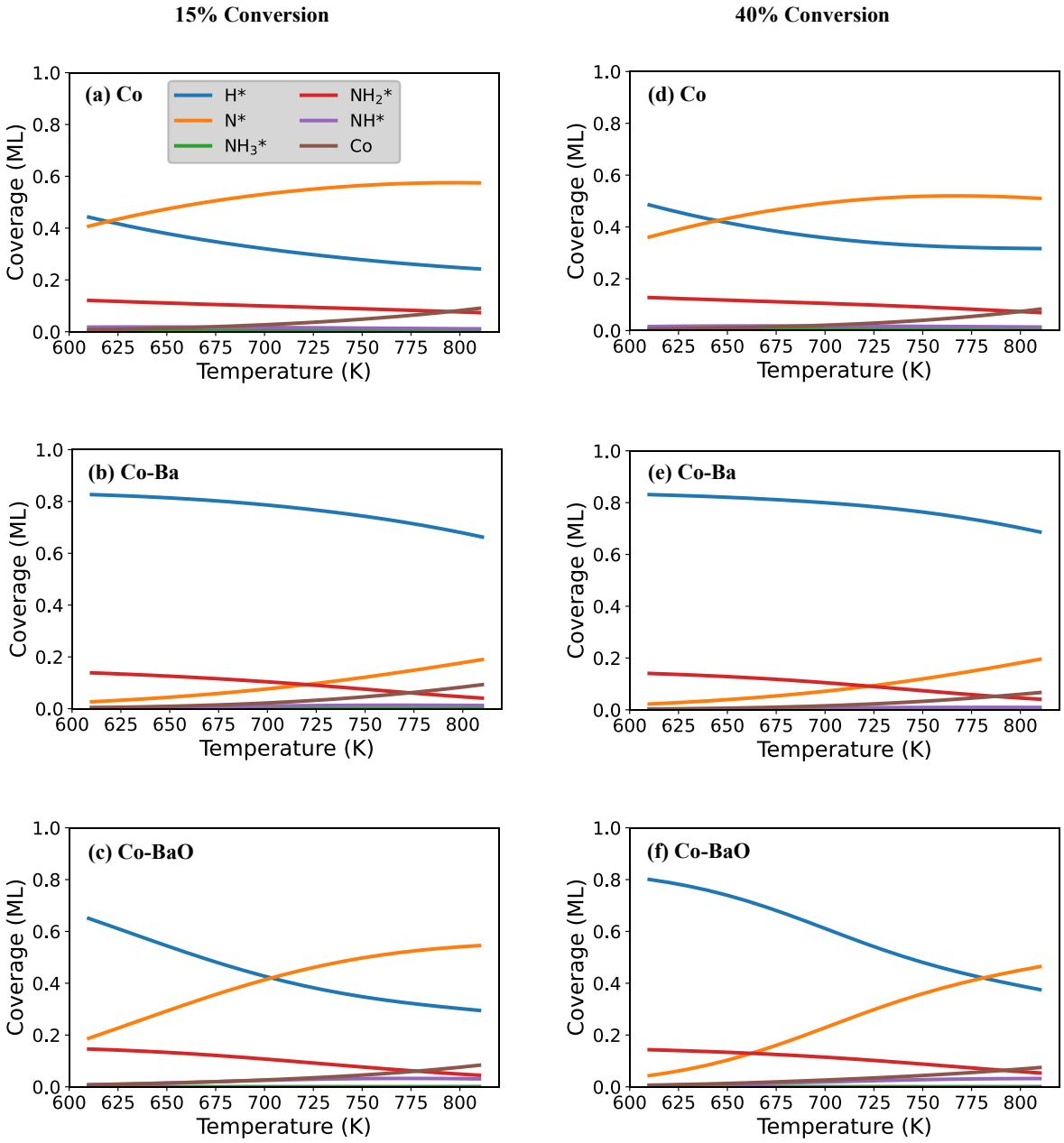


**Fig. 6.** Surface coverage distributions of reaction species for (a) Co, (b) Co-Ba, and (c) Co-BaO versus temperature at 15% conversion. (d) Co, (e) Co-Ba, and (f) Co-BaO versus temperature at

40% conversion. The simulations are obtained for ammonia decomposing on a bare surface. Different coverage distributions are observed upon introducing Ba and BaO on the surface.

Developing an accurate microkinetic model for ammonia decomposition is not straightforward and some challenges need to be addressed. Firstly, there is a risk of overestimating $NH_2$ coverage when using a single-site model, resulting in $NH_2$ dominating the surface over H and N (Fig. S4). This can be resolved by applying a two-site model and understanding that $NH_2$ adsorption is favored on the step sites rather than the terrace sites (as done in Figs. 5 and 6). Secondly, the observed discrepancy with experiments where hydrogen is not the most abundant species at low conversion (15%) introduces another layer of complexity. Navigating this issue requires a deeper look into how the surface coverage changes with conversion to ensure that the model presents the correct dominant species. Finally, the rates of promoted surfaces appear inaccurate in comparison to pristine Co. This warrants additional investigation, particularly due to the promoter-induced impact on H binding energies at high H coverage as shown in Fig. 3. Tackling these challenges is important to enhance the predictive capabilities of microkinetic models for the ammonia decomposition reaction.

*3.4. Coverage effect of H* on $NH_3$ adsorption*

Considering the expected influence of promoters on $H_2$ production rates, the results in Section 3.3 motivated a further look into the effect of H coverage on the surface. Calculations on a smaller unit cell of the $(10\bar{1}2)$ stepped Co surface showed similar energy barriers for $NH_3$ scission at different H coverages as shown in Table S10. As a result, the energy barriers for surface reactions were kept unchanged and only adsorption steps were modified and recalculated with the presence of H coverage.

The co-existence of $NH_3$ with high H coverage has not been evaluated in theoretical studies. Correspondingly, there is still uncertainty regarding whether promoters affect the adsorption of $NH_3$ differently when the surface is covered with H. The reason ammonia was selected among all the intermediates stems from its inherently weak adsorption compared to H (Table S11). To incorporate the coverage effect of H, the rates of $NH_3$ and H adsorption were recalculated with an initial coverage of 18 adsorbed H (0.75 ML) for Co, 12 adsorbed H (0.60 ML) for Co-Ba, and 14 adsorbed H (0.78 ML) for Co-BaO as shown in Fig. 7. These coverages correspond to the most thermodynamically stable coverages in Fig. 3 minus two H atoms. The most stable H coverages are 20 H atoms (0.83 ML) for Co, 14 H atoms (0.70 ML) for Co-Ba, and 16 H atoms (0.89 ML) for Co-BaO as shown in Fig. 3. Two H atoms are removed to enable the adsorption of two additional H atoms (the reverse reaction of Step 6).

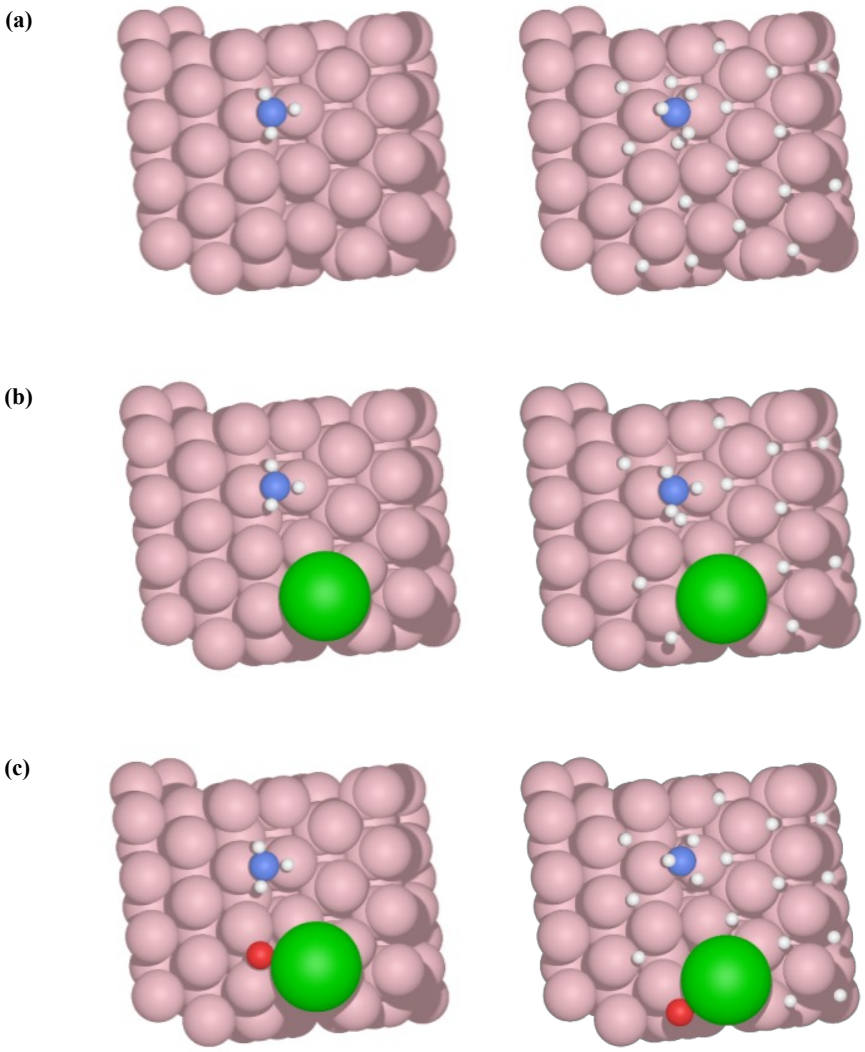


**Fig. 7.** Structures for the adsorption of $NH_3$ on bare and H-covered surfaces of (a) Co (18 H), (b) Co-Ba (12 H), and (c) Co-BaO (14 H). Color code: Co (pink), Ba (green), O (red), N (blue), and H (white).

Table 2 presents the adsorption Gibbs free energy values of H and $NH_3$ used on the bare surface model and the H-covered model. The H-covered model employs differential adsorption energies of H and $NH_3$ with respect to H-covered surfaces. While the variations in the differential adsorption of H may seem subtle (Table 2), the H coverage significantly influences

the adsorption of $NH_3$ from exothermic (on bare surface) to endothermic (on H-covered surfaces). Even though Co-Ba and Co-BaO initially exhibited comparable adsorption energies of ammonia on bare surfaces (Fig. 2), the effect of the strong H adsorption on Co-Ba becomes apparent when the surface is saturated with H atoms. Overall, the adsorption energies are weaker with the presence of H on the surface.

**Table 2**

Adsorption Gibbs free energy (eV) at 723.15 K for $NH_3$ and H on bare and H-covered Co (18 H), Co-Ba (12 H), and Co-BaO (14 H).

| | **Co** | | **Co-Ba** | | **Co-BaO** | |
|---|---|---|---|---|---|---|
| Surface | Bare | H-covered | Bare | H-covered | Bare | H-covered |
| $NH_3$ | −0.21 | −0.01 | −0.01 | 0.29 | −0.01 | 0.15 |
| H | −0.18 | −0.04 | −0.25 | −0.07 | −0.20 | −0.05 |

Fig. 8 shows the $H_2$ production rates for H-covered Co, Co-Ba, and Co-BaO at various temperatures. Co-Ba shows a higher rate at lower temperatures. However, as the temperature increases, both Co and Co-BaO outperform Co-Ba. Conversely, Co exhibits a higher rate when the temperature exceeds 750 K because the adsorption of ammonia for the Ba-promoted surfaces becomes challenging at higher temperatures (Table 2), which makes the rates relatively slow. At the reaction temperature, Co-BaO shows a higher production rate than Co and Co-Ba. The superiority of Co-BaO can be attributed to a lower transition state than Co for the N–N association step, coupled with a lesser impact of H coverage than Co-Ba on weakening the adsorption of ammonia. The coverage distribution at various temperatures for the vacant sites that are not pre-covered with H is shown in Fig. S5.

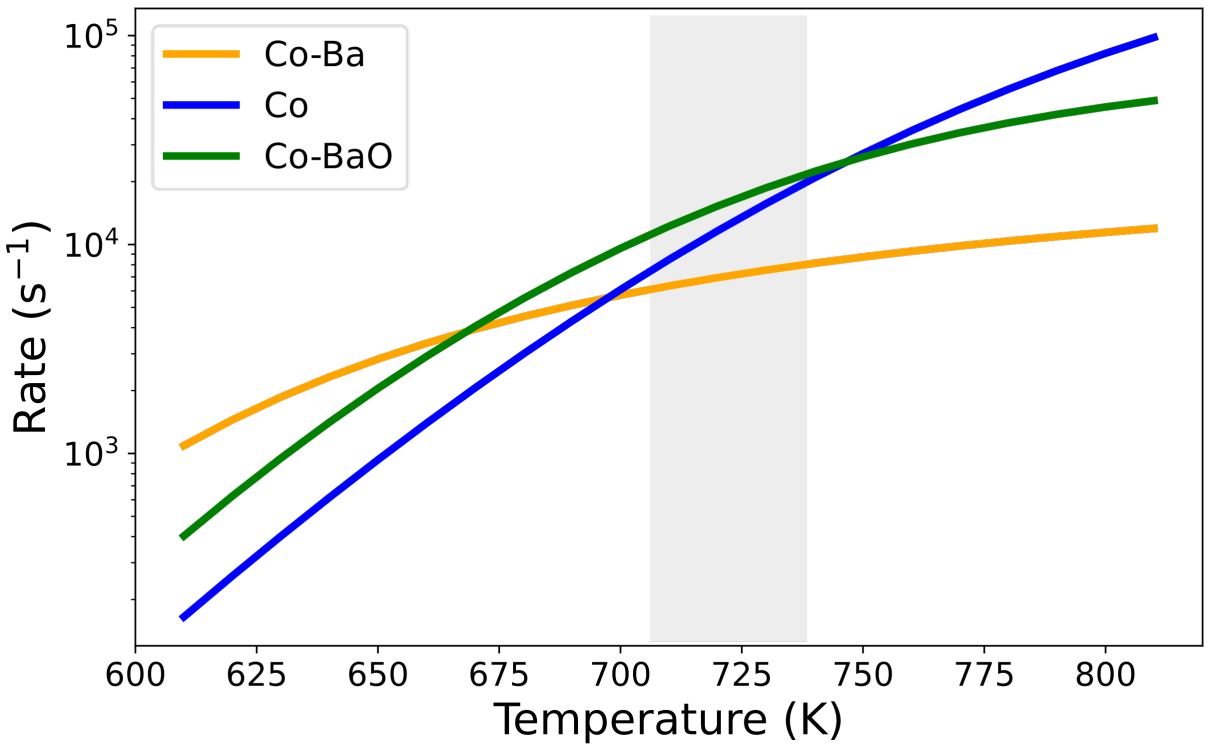


**Fig. 8.** $H_2$ production rates ($s^{-1}$) of H-covered Co, Co-Ba, and Co-BaO versus temperature (K) at 15% conversion, from microkinetic simulations using adsorption energies calculated at high H coverage. The gray shaded area indicates the reaction temperature (723.15 K). Co-BaO shows a higher production rate. The competitive adsorption of H is blocking the adsorption of ammonia on Co-Ba.

To determine how each of the energy barriers influences the rate of $H_2$ production, the degree of rate control (DRC) was calculated for the activated surface reaction elementary steps and presented in Fig. 9. For Co and Co-BaO, $NH_2$ dehydrogenation and N–N association have the largest positive DRC values as shown in Fig. 9(a and c). However, between these two steps, N–N association has the largest DRC. Unlike the cases for Co and Co-BaO, Co-Ba showed a single dominating step with a positive DRC value, which is $NH_3$ dehydrogenation as shown in Fig. 9(b). The switch in the rate-determining step (RDS) to $NH_3$ dehydrogenation for Co-Ba is

attributed to the Ba promotional effect on the N–N association and the second N–H bond-breaking steps. The findings in Fig. 9 are consistent with the calculated reaction profiles in Fig. 4, as both the N–N association (TS4) and the second dehydrogenation step (TS2) represent the highest free energies in the pathway for Co and Co-BaO. In contrast, for Co-Ba, the $NH_3$ dehydrogenation barrier (TS1) is the highest transition state in free energy (Fig. 4).

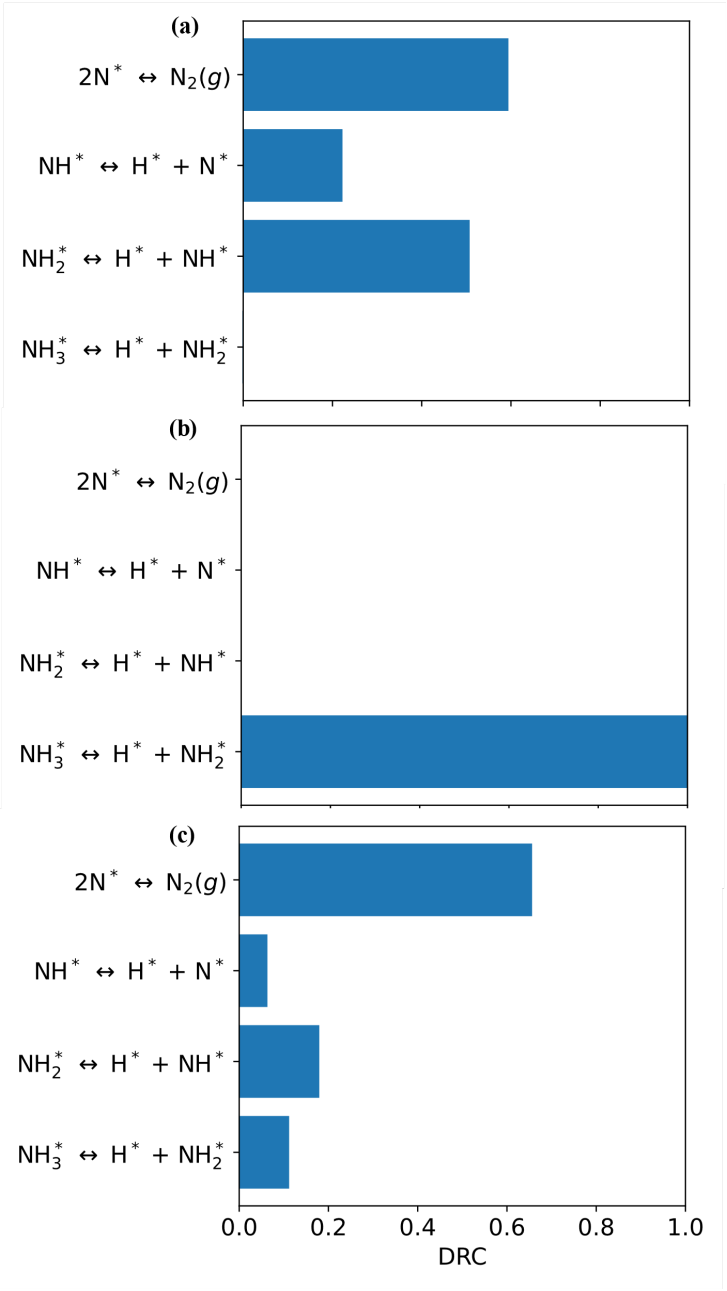


**Fig. 9.** Degree of rate control (DRC) of the activated reaction steps for ammonia decomposition on (a) Co, (b) Co-Ba, and (c) Co-BaO at 723.15 K and 15% conversion. N–N association has the largest positive DRC value for Co and Co-BaO, while the dehydrogenation of ammonia has the largest DRC value for Co-Ba.

The kinetic analysis of experimental results of Ba-promoted Co catalysts proposed that N–N association and $NH_2$ scission are both kinetically relevant steps in the reaction, with N–N association as the RDS and $NH_2$ scission representing a relatively slow step [26]. Therefore, the computed kinetic analysis of the influence of Ba and BaO on the Co surface presented in Figs. 8 and 9 shows that Co-BaO aligns more closely with experimental observations than Co-Ba. This implies that the Ba on the Co surface is likely to be O-bound. This is in line with the surface stability diagram in Fig. S1, which shows that the Co-BaO catalyst is more stable than Co-Ba.

*3.5. Electronic origin of promoter effect*

It has been reported in the literature that certain adsorbed promoters, including Ba, decrease the spin moment of the Co atoms in their immediate vicinity, resulting in a stabilized N–N transition state [32,33]. Table 3 shows the difference in spin moment when $N_2$ was adsorbed on CoBa and Co-BaO relative to $N_2$ on pristine Co. These local spin moments are obtained by taking the difference between the up and the down spin charges. The reduction in the spin moment between Co-BaO and Co is insignificant, which could explain why they have similar N–N association barriers. Meanwhile, the reduction in spin moment induced by metallic Ba is evident, explaining the reduced barrier of N–N association as shown in Table 3. The reduction in Co spin moment can explain the effect of metallic Ba, but this explanation does not apply to the case of BaO, which is the relevant situation under experimental conditions.

**Table 3**

Δ Spin moment (μB) of $N_2$ on CoBa and Co-BaO relative to $N_2$ on pristine Co on neighboring Co atoms and the promotion effect on the N–N association energy barrier.

| | Co-Ba | Co-BaO |
|---|---|---|
| Δ spin moment (μB) of step Co | 0.115 | −0.011 |
| Δ spin moment (μB) of terrace Co | 0.095 | 0.008 |
| $\Delta E_{\text{N–N TS}}$ (eV) | −0.23 | 0.00 |

To further examine the electronic properties, Bader charge and density of states (DOS) were calculated and presented in Fig. 10(a) and Fig. S6. Bader charge analysis revealed that O from BaO induces a positive charge on the adjacent Co atom ($Co^b$). This positive charge contributes to the weakened adsorption energy for the adsorbates located in a bridge site that includes this Co atom. There is an upward shift of the *d*-band center with respect to the Fermi level in the case of Co-Ba and Co-BaO relative to pristine Co. The shift induced by BaO is less significant than that induced by Ba, indicating that another effect might have a greater impact (Fig. S6 and Table S12).

The electrostatic field induced by Ba and BaO, indicating the presence of ionic bonding as reported previously for other alkali promoters, was determined [59]. The average electrostatic potential along a line perpendicular to the Co surface is shown in Fig. S7. To determine the value of the promoter-induced electrical field ($\varepsilon_{\text{promoter}}$), the slope of the difference in average electrostatic potential relative to the surface of pristine Co was calculated as shown in Fig. 10(b). $\varepsilon_{\text{promoter}}$ of Co-BaO is larger than that of Co-Ba, which indicates that the promotional effect of BaO is primarily dictated by the induced electrostatic potential. This finding emphasizes the

significance of considering the electrostatic influence of BaO-doped Co catalysts and paves the way for a more comprehensive understanding of the effects of promoters.

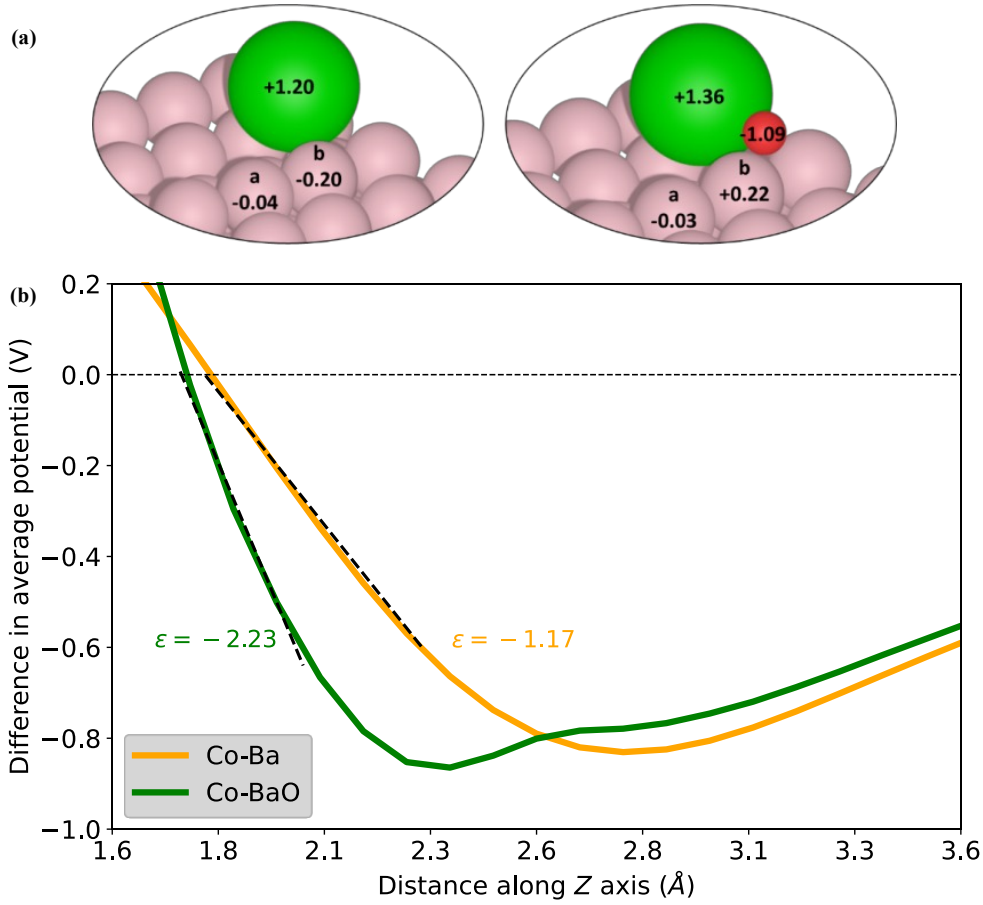


**Fig. 10.** (a) Bader charge analysis of the corresponding Co atoms labeled a and b. O induces a positive charge on the adjacent Co atom ($Co^{b}$). Color code: Co surface (pink), Ba (green), and O (red). (b) Difference in average electrostatic potential (V) of Co-Ba and Co-BaO with respect to pristine Co along a line perpendicular to the Co surface. The promoter-induced electrical field ($\varepsilon$ (V/Å)) is the slope of the black dotted line along the curve. $\varepsilon_{promoter}$ of Co-BaO is larger than that of Co-Ba, implying that the promotional effect of BaO is controlled to a larger extent by the induced electrostatic potential.

## 4. Conclusions

This study provides insights into the promotion mechanism of Ba-doped Co catalysts for the ammonia dehydrogenation reaction and the role of promoters in alleviating the competitive adsorption of H on the catalytic surface. First, the importance of studying the coverage effect on adsorption energies was highlighted in this study. A distinct contrast between Co, Co-Ba, and Co-BaO appeared only when multiple H atoms were adsorbed. The weakened adsorption of H on Co-BaO hints at the active role of BaO in mitigating the competitive adsorption of H.

Free energy reaction profiles were calculated to study the influence of Ba and BaO on N–H bond-breaking and N–N association steps. The full reaction pathway was calculated, which revealed that limiting the investigation to the N–N association step overlooks the promotional effect on the $NH_x$ dehydrogenation steps.

Microkinetic simulations were then constructed based on the free energy reaction profiles. Challenges of modelling the ammonia decomposition reaction were addressed by applying a two-site model and understanding that $NH_2$ adsorption is favored on the step sites rather than the terrace sites. When the effect of H coverage was not considered in the microkinetic simulations, Co showed the highest rate compared to Ba-promoted catalysts. This conflicted with the experimental results. On the other hand, the microkinetic simulations based on adsorption energies with high H coverage agreed with the experimental results and showed that Co-BaO exhibited higher activity than Co-Ba and Co under reaction conditions. The origin of the higher activity of Co-BaO stems from the lower transition state for the N–N association step compared to Co, coupled with a reduced impact of the H coverage on weakening ammonia adsorption compared to Co-Ba. High endergonic adsorption of ammonia was observed for H-covered Co-Ba at the reaction temperature, which made the rate relatively slow. N–N association

was the RDS for Co and Co-BaO, and $NH_2$ dehydrogenation was a slow step. While for Co-Ba, the $NH_3$ dehydrogenation is the RDS. The switch in the RDS to $NH_3$ dehydrogenation for Co-Ba was attributed to the Ba promotional effect on the N–N association. The kinetic analysis of the influence of Ba and BaO on the Co surface showed that Co-BaO aligns more closely with experimental observations than Co-Ba. This implies that the Ba on the Co surface is likely to be O-bound. The reduced barrier for N–N association in Co-Ba was attributed to the reduction in spin moment in the case of metallic Ba, while the reduction in the spin moment between Co-BaO and Co is insignificant and the promotional effect of BaO is predominantly driven by the electrostatic potential. Understanding the kinetics of decomposing ammonia provides a foundation for developing highly effective catalytic systems to utilize ammonia as a carrier for hydrogen, setting the stage for a sustainable energy landscape.

## CRediT authorship contribution statement

**Zahra Almisbaa:** Conceptualization, Formal analysis, Investigation, Writing – original draft, Funding acquisition. **Philippe Sautet:** Writing – review & editing, Funding acquisition, Supervision.

## Declaration of competing interest

The authors declare that they have no known competing financial interests or personal relationships that could have appeared to influence the work reported in this paper.

## Acknowledgments

Z.A. gratefully acknowledges Saudi Aramco for their funding. The authors are grateful to Prof. Jorge Gascon, Dr. George Yan and Dr. Hassan Aljama for the fruitful discussions. This work was supported by the Supercomputing Laboratory at King Abdullah University of Science & Technology (KAUST) in Thuwal, Saudi Arabia. This work also used Expanse cluster at San Diego Supercomputer Center through allocation TG-CHE170060 from the Advanced Cyberinfrastructure Coordination Ecosystem: Services & Support (ACCESS) program, which is supported by National Science Foundation grants #2138259, #2138286, #2138307, #2137603, and #2138296.

## Appendix A. Supplementary material

Gas phase thermodynamics, generated geometries for coverage-dependent H adsorption, energy barriers for the elementary steps, initial, transition and final states structures, spin and non-spin polarized chemisorption energies, average electrostatic potential.

## References


[1] S. Mateti, L. Saranya, G. Sathikumar, Q. Cai, Y. Yao, Y.I. Chen, Nanotechnology 33 (2022) 222001.

[2] S. Sun, Q. Jiang, D. Zhao, T. Cao, H. Sha, C. Zhang, H. Song, Z. Da, Renew. Sustain. Energy Rev. 169 (2022) 112918.

[3] M. Aziz, A. TriWijayanta, A.B.D. Nandiyanto, Energies 13 (2020) 1–25.

[4] S. Ristig, M. Poschmann, J. Folke, O. Gómez-Cápiro, Z. Chen, N. Sanchez-Bastardo, R. Schlögl, S. Heumann, H. Ruland, Chemie-Ingenieur-Technik 94 (2022) 1413–1425.

[5] L.C. Caballero, N.E. Thornburg, M.M. Nigra, Chem. Sci. 13 (2022) 12945–12956.

[6] S. Peters, A.M. Abdel- Mageed, S. Wohlrab, ChemCatChem 15 (2023) e202201185.

[7] H. Yousefi Rizi, D. Shin, Energies 15 (2022) 8246.

[8] E. Spatolisano, L.A. Pellegrini, A.R. de Angelis, S. Cattaneo, E. Roccaro, Ind. Eng. Chem. Res. 62 (2023) 10813–10827.

[9] N. Morlanés, S. Sayas, G. Shterk, S.P. Katikaneni, A. Harale, B. Solami, J. Gascon, Catal. Sci. Technol. 11 (2021) 3014–3024.

[10] G. Thomas, G. Parks, Potential Roles of Ammonia in a Hydrogen Economy. U.S. Department of Energy, 2006.

[11] N. Realpe, S.R. Kulkarni, J.L. Cerrillo, N. Morlanés, G. Lezcano, S.P. Katikaneni, S.N. Paglieri, M. Rakib, B. Solami, J. Gascon, P. Castaño, React. Chem. Eng. 8 (2023) 989–1004.

[12] F.R. García-García, A. Guerrero-Ruiz, I. Rodríguez-Ramos, Top. Catal. 52 (2009) 758–764.

[13] H.B. Kim, E.D. Park, Catal. Today 411–412 (2023) 113817.

[14] V. Prasad, A.M. Karim, A. Arya, D.G. Vlachos, Ind. Eng. Chem. Res. 48 (2009) 5255–5265.

[15] S.R. Kulkarni, N. Realpe, A. Yerrayya, V.K. Velisoju, S. Sayas, N. Morlanes, J. Cerillo, S.P. Katikaneni, S.N. Paglieri, B. Solami, J. Gascon, P. Castaño, Catal. Sci. Technol. 13 (2023) 2026–2037.

[16] S. Sayas, N. Morlanés, S.P. Katikaneni, A. Harale, B. Solami, J. Gascon, Catal. Sci. Technol. 10 (2020) 5027–5035.

[17] K. Kishida, M. Kitano, Y. Inoue, M. Sasase, T. Nakao, T. Tada, H. Abe, Y. Niwa, T. Yokoyama, M. Hara, H. Hosono, Chem. - A Eur. J. 24 (2018) 7976–7984.

[18] T.E. Bell, L. Torrente-Murciano, Top. Catal. 59 (2016) 1438–1457.

[19] A. Srifa, K. Okura, T. Okanishi, H. Muroyama, T. Matsui, K. Eguchi, Appl. Catal. B Environ. 218 (2017) 1–8.

[20] P. Xie, Y. Yao, Z. Huang, Z. Liu, J. Zhang, T. Li, G. Wang, R. Shahbazian-Yassar, L. Hu, C. Wang, Nat. Commun. 10 (2019) 1–12.

[21] B.-Y. Zhang, P.-P. Chen, J.-X. Liu, H.-Y. Su, W.-X. Li, J. Phys. Chem. C 123 (2019) 10956–10966.

[22] H.Y. Su, Y. Zhao, J.X. Liu, K. Sun, W.X. Li, Catal. Sci. Technol. 7 (2017) 2967–2977.

[23] S. Dahl, P.A. Taylor, E. Törnqvist, I. Chorkendorff, J. Catal. 178 (1998) 679–686.

[24] F. Chang, J. Guo, G. Wu, L. Liu, M. Zhang, T. He, P. Wang, P. Yu, P. Chen, RSC Adv. 5 (2015) 3605–3610.

[25] V. Shadravan, A. Cao, V.J. Bukas, M.K. Grønborg, C.D. Damsgaard, Z. Wang, J. Kibsgaard, J.K. Nørskov, I. Chorkendorff, Energy Environ. Sci. 15 (2022) 3310–3320.

[26] G. Lezcano, N. Realpe, S.R. Kulkarni, S. Sayas, J. Cerrillo, N. Morlanes, H.O. Mohamed, V.K.

Velisoju, R.F. Aldilajan, S.P. Katikaneni, M. Rakib, B. Solami, J. Gascon, P. Castaño, Chem. Eng. J. 471 (2023) 144623.

[27] Y. Qiu, E. Fu, F. Gong, R. Xiao, Int. J. Hydrogen Energy 47 (2022) 5044–5052.

[28] A. Takahashi, T. Fujitani, J. Chem. Eng. Japan 49 (2016) 22–28.

[29] Z. Wang, Z. Cai, Z. Wei, ACS Sustain. Chem. Eng. 7 (2019) 8226–8235.

[30] D.S. Rivera Rocabado, T. Ishimoto, M. Aizawa, T.G. Noguchi, M. Yamauchi, Catalysts 12 (2022) 1–12.

[31] H. He, H. Jiang, F. Yang, J. Liu, W. Zhang, M. Jin, Z. Li, Int. J. Hydrogen Energy 48 (2023) 5030–5041.

[32] A. Cao, V.J. Bukas, V. Shadravan, Z. Wang, H. Li, J. Kibsgaard, I. Chorkendorff, J.K. Nørskov, Nat. Commun. 13 (2022) 2382.

[33] A. Cao, J.K. Nørskov, ACS Catal. 13 (2023) 3456–3462.

[34] J. Qian, Q. An, A. Fortunelli, R.J. Nielsen, W.A. Goddard, J. Am. Chem. Soc. 140 (2018) 6288–6297.

[35] G. Xu, C. Cai, T. Wang, J. Am. Chem. Soc. 144 (2022) 23089–23095.

[36] G. Kresse, J. Furthmuller, Comput. Mater. Sci. 6 (1996) 15–50.

[37] G. Kresse, Phys. Rev. B 54 (1996) 11169–11186.

[38] Sree Harsha Bhimineni, GitHub (2023).

[39] G. Kresse, D. Joubert, Phys. Rev. B 59 (1999) 1758–1775.

[40] P.E. Blochl, Phys. Rev. B 50 (1994) 17953–17979.

[41] J.P. Perdew, K. Burke, M. Ernzerhof, Phys. Rev. Lett. 77 (1996) 3865–3868.

[42] S. Grimme, J. Antony, S. Ehrlich, H. Krieg, J. Chem. Phys 132 (2010) 154104.

[43] S. Grimme, S. Ehrlich, L. Goerigk, J. Comput. Chem. 32 (2011) 1456–1465.

[44] C.J. Weststrate, M. Mahmoodinia, M.H. Farstad, I.H. Svenum, M.D. Strømsheim, J.W. Niemantsverdriet, H.J. Venvik, Catal. Today 342 (2020) 124–130.

[45] L. Liu, C. Qin, M. Yu, Q. Wang, J. Wang, B. Hou, L. Jia, D. Li, ChemCatChem 12 (2020) 2083–2090.

[46] Q. Chen, I.H. Svenum, Y. Qi, L. Gavrilovic, D. Chen, A. Holmen, E.A. Blekkan, Phys. Chem. Chem. Phys. 19 (2017) 12246–12254.

[47] Q. Chen, I.H. Svenum, L. Gavrilovic, D. Chen, E.A. Blekkan, Surf. Sci. 681 (2019) 24–31.

[48] H.J. Monkhorst, J.D. Pack, Phys. Rev. B 13 (1976) 5188–5192.

[49] G. Henkelman, B.P. Uberuaga, H. Jónsson, J. Chem. Phys. 113 (2000) 9901–9904.

[50] C. Huo, B. Wu, P. Gao, Y. Yang, Y. Li, H. Jiao, Angew. Chemie Int. Ed. 50 (2011) 7403–7406.

[51] A. Hjorth Larsen, J. Jørgen Mortensen, J. Blomqvist, I.E. Castelli, R. Christensen, M. Dułak, J. Friis, M.N. Groves, B. Hammer, C. Hargus, E.D. Hermes, P.C. Jennings, P. Bjerre Jensen, J. Kermode, J.R. Kitchin, E. Leonhard Kolsbjerg, J. Kubal, K. Kaasbjerg, S. Lysgaard, J. Bergmann Maronsson, T. Maxson, T. Olsen, L. Pastewka, A. Peterson, C. Rostgaard, J. Schiøtz, O. Schütt, M. Strange, K.S. Thygesen, T. Vegge, L. Vilhelmsen, M. Walter, Z. Zeng, K.W. Jacobsen, J. Phys. Condens. Matter 29 (2017) 273002.

[52] P. Virtanen, R. Gommers, T.E. Oliphant, M. Haberland, T. Reddy, D. Cournapeau, E. Burovski, P. Peterson, W. Weckesser, J. Bright, S.J. van der Walt, M. Brett, J. Wilson, K.J. Millman, N. Mayorov, A.R.J. Nelson, E. Jones, R. Kern, E. Larson, C.J. Carey, İ. Polat, Y. Feng, E.W. Moore, J. VanderPlas, D. Laxalde, J. Perktold, R. Cimrman, I. Henriksen, E.A. Quintero, C.R. Harris,

A.M. Archibald, A.H. Ribeiro, F. Pedregosa, P. van Mulbregt, A. Vijaykumar, A. Pietro Bardelli, A. Rothberg, A. Hilboll, A. Kloeckner, A. Scopatz, A. Lee, A. Rokem, C.N. Woods, C. Fulton, C. Masson, C. Häggström, C. Fitzgerald, D.A. Nicholson, D.R. Hagen, D. V. Pasechnik, E. Olivetti, E. Martin, E. Wieser, F. Silva, F. Lenders, F. Wilhelm, G. Young, G.A. Price, G.-L. Ingold, G.E. Allen, G.R. Lee, H. Audren, I. Probst, J.P. Dietrich, J. Silterra, J.T. Webber, J. Slavič, J. Nothman, J. Buchner, J. Kulick, J.L. Schönberger, J.V. de Miranda Cardoso, J. Reimer, J. Harrington, J.L.C. Rodríguez, J. Nunez-Iglesias, J. Kuczynski, K. Tritz, M. Thoma, M. Newville, M. Kümmerer, M. Bolingbroke, M. Tartre, M. Pak, N.J. Smith, N. Nowaczyk, N. Shebanov, O. Pavlyk, P.A. Brodtkorb, P. Lee, R.T. McGibbon, R. Feldbauer, S. Lewis, S. Tygier, S. Sievert, S. Vigna, S. Peterson, S. More, T. Pudlik, T. Oshima, T.J. Pingel, T.P. Robitaille, T. Spura, T.R. Jones, T. Cera, T. Leslie, T. Zito, T. Krauss, U. Upadhyay, Y.O. Halchenko, Y. Vázquez-Baeza, Nat. Methods 17 (2020) 261–272.

[53] A. Vojvodic, A.J. Medford, F. Studt, F. Abild-Pedersen, T.S. Khan, T. Bligaard, J.K. Nørskov, Chem. Phys. Lett. 598 (2014) 108–112.

[54] A.A. Gokhale, S. Kandoi, J.P. Greeley, M. Mavrikakis, J.A. Dumesic, Chem. Eng. Sci. 59 (2004) 4679–4691.

[55] T. Wang, J. Ibañez, K. Wang, L. Fang, M. Sabbe, C. Michel, S. Paul, M. Pera-Titus, P. Sautet, Nat. Catal. 2 (2019) 773–779.

[56] A.B. Mhadeshwar, J.R. Kitchin, M.A. Barteau, D.G. Vlachos, Catal. Letters 96 (2004) 13–22.

[57] D.A. Hansgen, D.G. Vlachos, J.G. Chen, Nat. Chem. 2 (2010) 484–489.

[58] Z. Almisbaa, H.A. Aljama, K. Almajnouni, L. Cavallo, P. Sautet, ACS Catal. 13 (2023) 7358–7370.

[59] B. Hammer, J.K.K. Nørskov, Adv. Catal. 45 (2000) 71–129.

## Graphical Abstract

The modified adsorption properties of Co upon the addition of metallic Ba and BaO suggest that BaO plays a role in alleviating the competitive adsorption of H.